Ultrafast Electronic and Structural Response of Monolayer MoS_2 under Intense Photoexcitation Conditions

Ehren M. Mannebach,[†] Karel-Alexander N. Duerloo,[†] Lenson A. Pellouchoud,[†] Meng-Ju Sher,[‡] Sanghee Nah,[†,‡] Yi-Hong Kuo,[§] Yifei Yu,[⊥] Ann F. Marshall,[∥] Linyou Cao,[⊥] Evan J. Reed,[†] and Aaron M. Lindenberg[*,†,‡,#]

[†]Department of Materials Science and Engineering, Stanford University, Stanford, California 94305, United States, [‡]Stanford Institute for Materials and Energy Sciences, SLAC National Accelerator Laboratory, Menlo Park, California 94025, United States, [§]Department of Electrical Engineering, Stanford University, Stanford, California 94305, United States, [⊥]Department of Materials Science and Engineering, North Carolina State University, Raleigh, North Carolina 27695, United States, [∥]Stanford Nanocharacterization Laboratory, Stanford University, Stanford, California 94305, United States, and [#]PULSE Institute, SLAC National Accelerator Laboratory, Menlo Park, California 94025, United States

ABSTRACT We report on the dynamical response of single layer transition metal dichalcogenide MoS_2 to intense above-bandgap photoexcitation using the nonlinear-optical second order susceptibility as a direct probe of the electronic and structural dynamics. Excitation conditions corresponding to the order of one electron–hole pair per unit cell generate unexpected increases in the second harmonic from monolayer films, occurring on few picosecond time-scales. These large amplitude changes recover on tens of picosecond time-scales and are reversible at megahertz repetition rates with no photoinduced change in lattice symmetry observed despite the extreme excitation conditions.

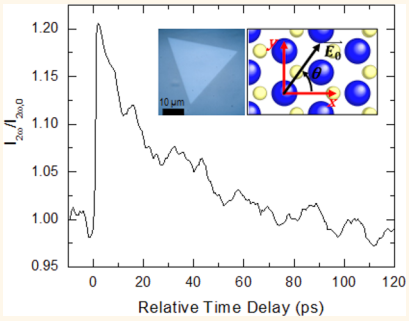

KEYWORDS: molybdenum disulfide · MoS_2 · second harmonic generation · ultrafast dynamics · monolayer · femtosecond

Intense efforts in the past few years have focused on the novel electronic, optical, and structural properties exhibited by molybdenum disulfide and related two-dimensional transition metal dichalcogenides. These include the emergence of a direct band gap,[1,2] strong light-matter interactions,[3,4] enhanced catalytic activity,[5,6] unique semiconducting and metallic structural phases controllable by strain,[5,7−10] and the ability to withstand extreme strains without plastic deformations.[11−14] 2D transition metal dichalcogenides typically consist of two hexagonal planes of chalcogen atoms separated by a hexagonal layer of metal atoms with trigonal prismatic coordination. Whereas bulk versions are centrosymmetric, inversion symmetry is broken for monolayers (and in general for odd numbers of layers), which results in novel valley-dependent selection rules,[15,16] as well as piezoelectric[17] and nonlinear optical responses[18,19] emergent in the single layer limit. Little is known about the dynamical electronic and structural processes that underlie these novel effects or the associated differences in the dynamics exhibited by few layer compared to bulk materials. In particular, the extreme stresses these materials are capable of withstanding point toward novel opportunities for dynamic control of these functional responses using light and other time-dependent stimuli. Although prior time-resolved optical pump–probe studies have investigated carrier relaxation and scattering processes at low photoexcitation conditions,[20−26] the electronic dynamics of two-dimensional systems have not been investigated in a regime associated with large amplitude strains, temperature jumps, or electronic excitation conditions, and the structural dynamics have not been probed at all. Here we present first measurements of the time-dependent structural and electronic response of 2D (single layer) MoS_2 following above-bandgap excitation at megahertz repetition rates, in a regime corresponding to of order one absorbed photon per unit cell

* Address correspondence to aaronl@stanford.edu.

Received for review August 9, 2014 and accepted September 22, 2014.

Published online September 22, 2014
10.1021/nn5044542

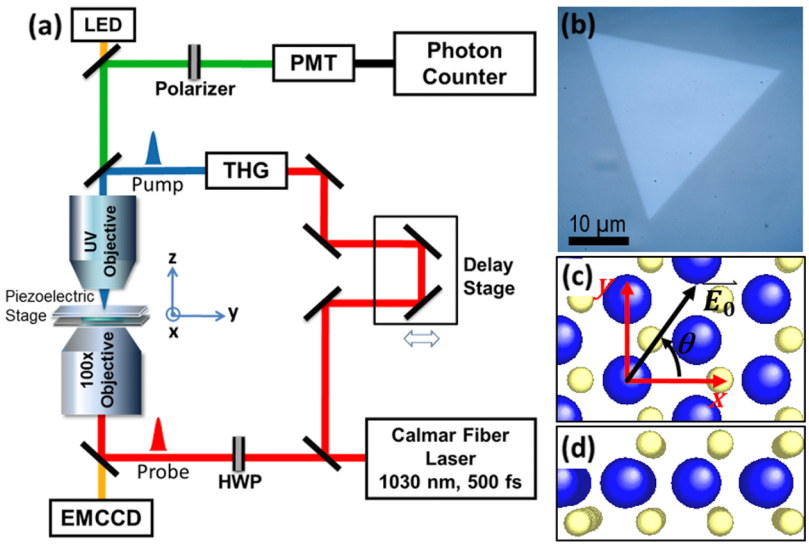

Figure 1. (a) Experimental schematic. 343 or 266 nm light is used to optically excite large-area monolayers of MoS_2, (b) and the time response of the second harmonic generation efficiency is measured. All experiments are done on single crystalline domains of monolayer MoS_2. (c) Top-view schematic of the MoS2 crystal structure with *x* and *y* axes labeled. Blue and yellow spheres correspond to Mo and S atoms, respectively. (d) Side-view along $\hat{y}$ (perpendicular to the plane of the paper) of the MoS_2 crystal structure.

($\sim 10^{15}$/cm^2, ~10% valence band excitation). These excitation conditions transform 2H-MoS_2 into a degenerate semiconductor/metal, with simple estimates of the transient lattice temperature jump of approximately 3000 K,[27] neglecting thermal conduction into the substrate and modifications in the linear optical properties. The associated dynamical response is probed using the second order nonlinear optical susceptibility as reflected in the second harmonic generated by the monolayer. This provides a direct crystallographically sensitive, all-optical probe of the trigonal symmetry of the material and its transient response. Despite these extreme excitation conditions, we observe large amplitude *increases* in the second harmonic generation occurring on few picosecond time-scales, indicative of the stability of these materials, with no evidence for disordering or melting responses as is observed in bulk semiconducting systems[28−30] under similar excitation conditions. Comparison with complementary measurements of the linear optical properties and with first-principles modeling of both the linear and nonlinear optical susceptibility show the observed effects can be associated with the extreme electronic temperatures induced without modification of the unit cell structure. The possibilities of optically inducing such large modifications to the electronic properties of these systems without concomitant structural changes open up new possibilities for reversible all-optical modulation and control of the optoelectronic properties of two-dimensional transition metal dichalcogenide materials under excitation conditions not sustainable in bulk systems.

RESULTS AND DISCUSSION

As reported previously by other groups,[18,19,31,32] we observe strong static second harmonic generation (SHG) from MoS_2 monolayers. A typical plot showing the dependence of the SHG intensity on the polarization of the incident probe light for a fixed output second harmonic (SH) polarization (either parallel or perpendicular to the experimental table, see Figure 1a) is given as Figure S1 (Supporting Information). The observed symmetry is consistent with the known D_{3h} symmetry group for monolayer 2H-MoS_2 with $I_x^{2\omega} \propto \cos^2(2\theta + \theta_0)$ and $I_y^{2\omega} \propto \sin^2(2\theta + \theta_0)$, where *x*, *y*, and θ are defined in Figure 1c, and θ_0 is a rotation of the MoS_2 crystallographic axes with respect to the *x*-direction.

Figure 2a shows the time-dependent response of the SHG efficiency (1030 nm probe) following above-bandgap photoexcitation with 343 nm light at ~10 mJ/cm^2. We observe an initial increase in the second harmonic of a few tens of percent that turns on within ~2 ps. Taking approximately known above-bandgap absorption coefficients of $\sim 10^6$ cm^{-1},[4] corresponding to an absorption of approximately 10% for a single monolayer, an excitation fluence of 10 mJ/cm^2 generates approximately 10^{15} e−h pairs/cm^2 ($\sim 10^{22}$ cm^{-3}), neglecting reflection losses. Under the approximation that carrier−carrier scattering equilibrates the electronic system at a well-defined electron temperature and quasi-Fermi level within a few hundred femtoseconds,[33] treating the electronic system as a degenerate 2D free electron gas then defines a quasi-Fermi energy $\varepsilon_F = \pi N\hbar^2/m \sim 2$ eV above the bottom of the conduction band, where *N* is the electron density.[34] Under the assumption of a parabolic band, equating the energy density of a 2D Fermi gas to the absorbed energy density then defines an electron temperature of ~1.4 eV = 16 000 K. These estimates are in agreement with density functional theory (DFT) calculations showing that carrier concentrations of 10^{15} cm^{-2}

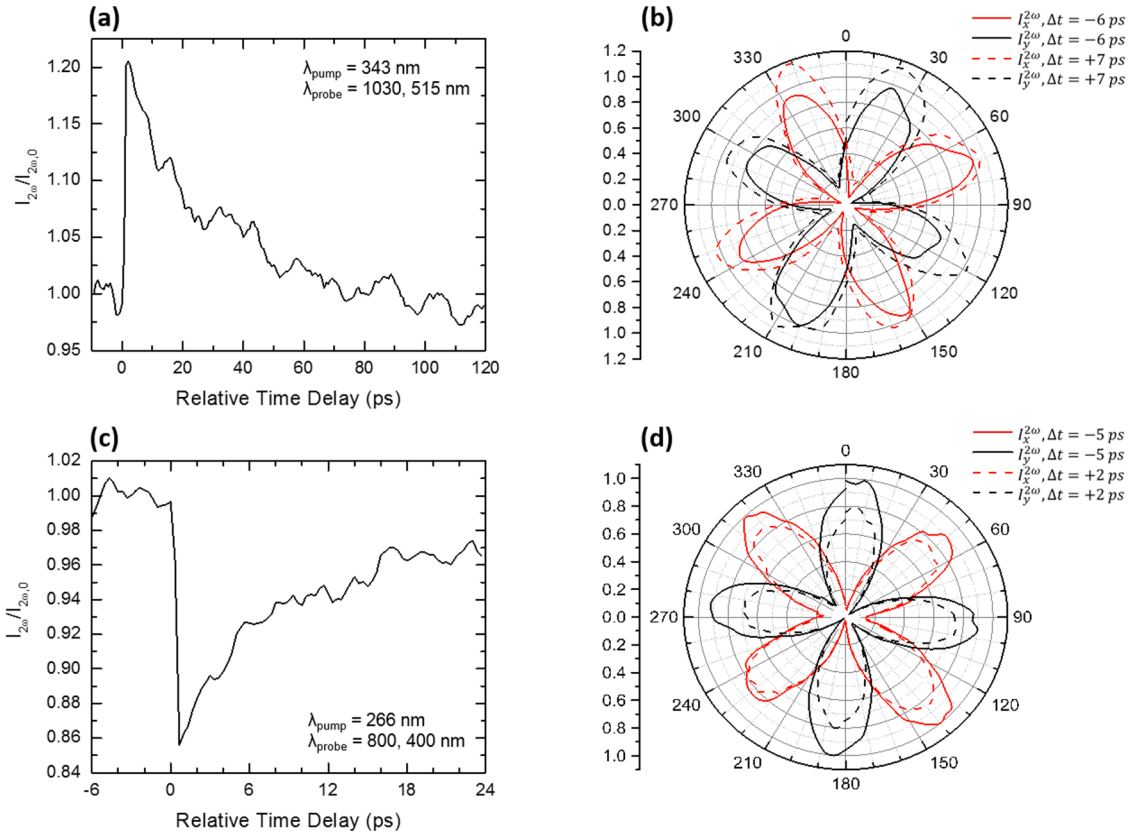

Figure 2. (a,c) Time-dependence of the SH response following above-bandgap excitation with 343 nm pump/1030 nm probe (a) and 266 nm pump/800 nm probe (c). In both cases, the effect reaches its maximum magnitude within the time resolution of the experiment. (b,d) Polarization dependence of the SH response before (solid lines) and after (dashed lines) above-bandgap excitation with 343 nm pump/1030 nm probe (b) and 266 nm pump/800 nm probe (d). The black and red data show *x*- and *y*-polarized SH light, respectively.

correspond to electron temperatures of ~10 000 K (Supporting Information). These conditions essentially define a quasi-half-filled conduction band and metallic-like characteristics, with interelectron spacing comparable to the electron de Broglie wavelength. Similar results are obtained treating the system as a 3D single layer of unit cells. Previous studies[28,30,35,36] have used the static second order susceptibility as a direct measure of photoinduced structural changes, observing large amplitude decreases in the SH under similar excitation conditions, associated with a transition from a noncentrosymmetric structure to a disordered or molten centrosymmetric one. The large-amplitude increases in SH and the fast recovery of the response indicate that these disordering effects are not relevant for monolayer MoS_2 despite the extreme excitation conditions utilized. This is further supported by the well-defined polarization dependence measured at t = 7 ps after time zero, showing no evidence for structural modulations, which would appear as a change in the symmetry of the polarization dependent plot (Figure 2b). Furthermore, a complex wavelength dependence of the induced changes in SH is observed. In contrast to the increase in SH signal seen in Figure 2a, the SHG response of an 800 nm probe beam is decreased by ~14% following above-bandgap excitation at 266 nm at ~10 mJ/cm^2 (Figure 2c), yielding similar densities of photoexcited carriers. Like the 1030 nm probe/343 nm pump conditions, the polarization traces before and after pumping (Figure 2d) change only in their magnitude, indicating that no structural transformation took place. The difference in recovery dynamics between the two probe conditions is likely explained by different carrier relaxation time scales at the two different second harmonic wavelengths, also observed when probing the linear optical properties (see Figure 4b,c and Figure S3d) as described below.

One can understand this unusual dynamical response by taking into the account the quasi-metallic-like state that is created at short times, and in particular, the dependence of the second-order nonlinear susceptibility on electron temperature. The second harmonic efficiency of a solid is often phenomenologically described in terms of contributions from valence band and conduction band states, reflecting bound and free charge contributions.[37−44] In metals, prior studies have shown an enhancement of the second harmonic efficiency with increasing electron temperature, dependent on the occupation of states within a partially filled

band.[37−39] In this model, the effective nonlinear susceptibility for the carriers is determined by considering this process as the absorption by a carrier of energy ε through two states of energy $\varepsilon + \hbar\omega$ and $\varepsilon + 2\hbar\omega$ followed by the subsequent re-emission of a photon at 2ω. The probability of this process will be proportional to the product $f(\varepsilon)[1 - f(\varepsilon - \hbar\omega)][1 - f(\varepsilon - 2\hbar\omega)][1 - f(\varepsilon)]$, where f is the Fermi−Dirac occupation factor, dependent on the electronic temperature. It is seen from this expression that this product increases as the distribution function broadens with increasing electron temperature, qualitatively explaining an effective increase of the susceptibility with electron temperature.

To investigate the potential magnitude of purely electronic changes in the SH response, we compute the linear susceptibility spectrum from first-principles and use the semiclassical two-point proportionality known as Miller's Rule.[45] This states that given a linear susceptibility spectrum, the second harmonic response follows $\chi^{(2)}(2\omega) \sim \chi^{(1)}(\omega)\chi^{(1)}(\omega)\chi^{(1)}(2\omega)$. The linear susceptibility can be derived for a set of independent electron wave functions, resulting in the well-known Kubo−Greenwood formula.[46] We utilize density functional theory (DFT) calculations as implemented in the Elk full-potential linearized augmented plane wave (FP-LAPW) code[47] to obtain independent electron (Kohn−Sham) wave functions. The wave functions are computed with self-consistent Fermi−Dirac occupancies for a given electronic temperature. Elk implements a perturbative approach for computing first-order (Kubo−Greenwood) and second-order optical coefficients from momentum matrix elements computed from these wave functions with Fermi−Dirac occupancies.[48] This approach neglects excitonic self-trapping of carriers and correlation effects that can play a role in the magnitude of quasiparticle gaps and other quantitative spectral features,[49,50] but is expected to provide qualitative guidance regarding trends with respect to electronic temperature.[51−53]

We have computed $\chi^{(1)}$ spectra and the corresponding Miller's Rule $\chi^{(2)}$ spectra for several electronic temperatures between 0 K and 16 000 K, the results of which are shown in Figure 3. We observe that at higher photon energies, Miller's Rule predicts a damping of the SH response with increasing electronic temperature. Below the calculated absorption edge, it is predicted that the SH response will increase dramatically with increasing electronic temperature, with percent-level changes comparable to those observed experimentally, associated with a strong increase in absorption below gap. The sub-bandgap absorption that is predicted to occur with increasing electronic temperature (Figure 3a, bottom) is seen in linear pump−probe experiments at optical and THz wavelengths, shown in Figures S3 and S5, further supporting this argument, and may be qualitatively understood in terms of interband excitations (within both valence and

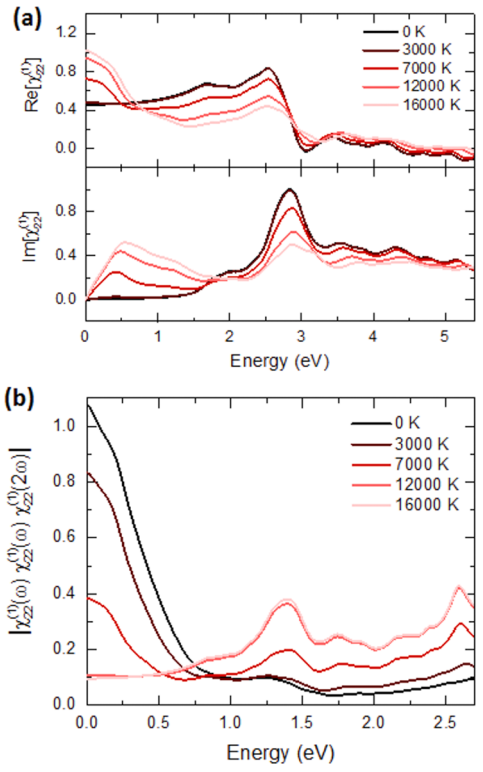

Figure 3. (a) Real (top) and imaginary (bottom) parts of the first order susceptibility, $\chi^{(1)}$. (b) Second harmonic optical response based on the Miller's Rule two-point proportionality to the first-order response spectra.

conduction bands) occurring as the electronic temperature increases and the distribution functions broaden. Additionally, the theory predicts that above a certain photon energy, an increase in electronic temperature leads to a damping of the SH response, consistent with the change in the sign of SHG modulation between the 1030 nm probe and 800 nm probe (Figure 2a,c). It is important to remember that the approach used in the calculations presented here only provide qualitative information concerning trends with changes in electronic temperature. Measurements of the modulation in the transmission (with $\Delta T/T \propto -\Delta\alpha/\alpha$) of the 500 and 400 nm linear probe beams (Figure 4) support the trends given by Miller's Rule: an increase in the absorption at 500 nm (*i.e.*, increase in $\chi^{(1)}(2\omega)$) gives rise to an increase in the second order susceptibility of MoS_2 at λ = 1030 nm. Likewise, a decrease in $\chi^{(1)}$ (400 nm) yields a decrease in $\chi^{(2)}$ (800 nm).

In addition to the Kubo−Greenwood-based Miller's Rule calculations, we have modified a portion of the Elk code to compute $\chi^{(2)}$ spectra with finite electron temperatures by perturbation theory. We expect these computations to provide a qualitative understanding analogous to the Kubo−Greenwood formula for the linear spectra,[54] and we note that both approaches employ DFT wave functions, lacking the excited-state electronic correlations that give accurate quasi-particle energies and electron−hole interactions that give rise

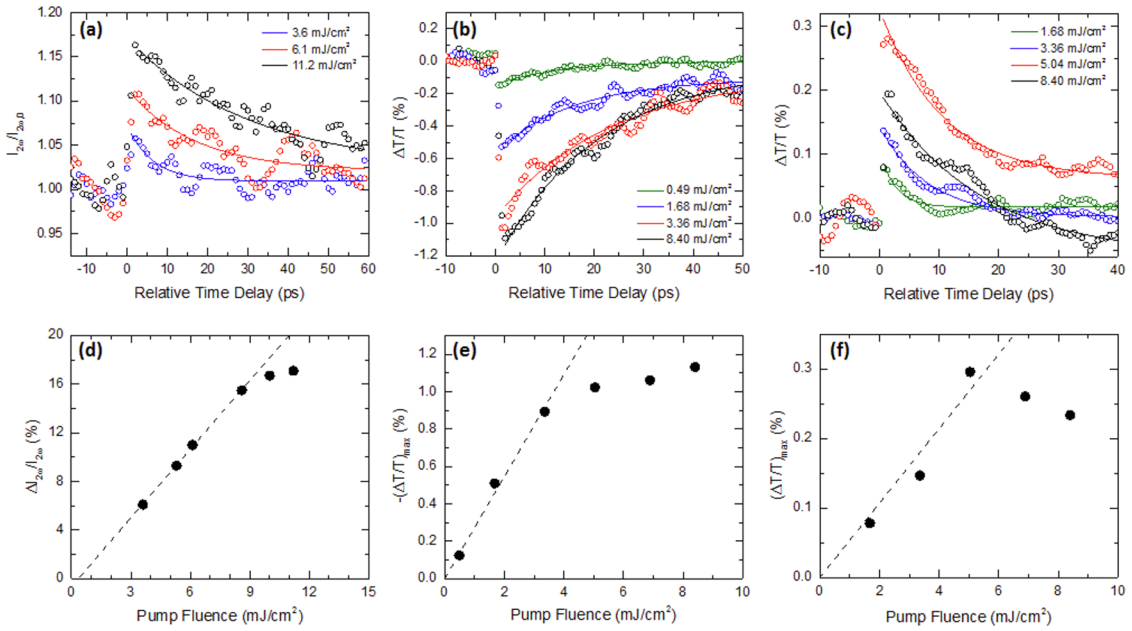

Figure 4. (a–c) Fluence dependence of the time-dependent SH response with 1030 nm probe (a) and linear absorption responses at 500 nm (b) and 400 nm (c) probe wavelengths. (d–f) Magnitude of the maximum change in SH (d), 500 nm absorption (e), and 400 nm absorption (f) as a function of above-bandgap excitation fluence. Some data sets are omitted from (a–c) for clarity.

to excitons. The computational cell of MoS_2 used for these calculations is described in detail in the Supporting Information, Part 4. With the atomic positions and computational cell fixed, we solved the DFT electronic system (density, independent electron wave functions, Fermi energy, and Fermi–Dirac occupancies) for several electronic temperatures between 0 K and 16 000 K. We then applied expression B1 from Hughes *et al.*[48] to obtain the $\chi^{(2)}$ spectra shown in Figure S6. While we expect the SHG efficiency to have a peak at half of the experimental direct optical gap (0.95 eV), the response based on DFT will arise at half of the DFT gap (0.85 eV). Figure S6 shows how transitions between pairs of valence states and between pairs of conduction states (all with fractional occupancy) give rise to a drastic increase in the SH response at low frequencies as electronic temperature increases, which is qualitatively similar to the results predicted using semiclassical Miller's Rule. At higher frequencies, the full perturbative approach yields a more nuanced behavior in the SH response with increasing electronic temperature than Miller's Rule, which predicts a monotonic damping of the SH response with increasing electronic temperature.

Further evidence for the claim that the modulations in the SH response are purely electronic in nature is obtained by examining the fluence dependence of the SH and linear optical time response as shown in Figure 4. Probing with a fundamental wavelength of 1030 nm, we observe a linear dependence of the magnitude of the increase in SHG with pump fluence until ~10 mJ/cm^2, at which point evidence for saturation is observed (Figure 4a,d). At these fluences, simple estimates show that approximately one photon is absorbed per unit cell, and one would expect both removal of valence band states and filling of conduction band states (*e.g.*, a Burstein–Moss shift) to lead to effects consistent with this observed saturation. Linear transmission measurements with a 400 nm pump beam (resonant with the C exciton, Figure S2) and 500 nm (Figure 4b,e) and 400 nm (Figure 4c,f) probe beams indicate evidence for saturable absorption at similar absorbed pump energies (Figure S2). For the 400 nm pump, 400 nm probe linear transmission measurements, a coherent interference effect at time zero was subtracted from the data (Supporting Information, Figure S4). We note that slow modulations observed in the data before and after time zero are likely associated with percent-level drifts in the laser power or detection electronics and not associated with acoustic responses.[55] It has also been reported[23] that dispersions of few-layer MoS_2 nanosheets (E_{gap} ~ 1.2 eV) exhibit saturable absorption of 800 nm (1.5 eV) light at fluences of ~40 mJ/cm^2. These results suggest that the apparent saturation in the magnitude of the increase in SHG from monolayer MoS_2 is due in part to saturable absorption of the 343 nm pump light and show that the SH response follows the linear optical response. Figure 5 directly shows that the modulation of the SH response and the linear transmission response at the corresponding SH wavelength relax on the same time scale. This is true for both the 1030 and 800 nm probes as shown in Figure 5a and Figure 5b, respectively, and is in accordance with the argument that the SH measurements are sensitive to carrier cooling and Miller's Rule. In both wavelength sets displayed in Figure 5, pump fluences were chosen so

that the absorbed energy per pump pulse was similar (Figure S2). This is important in particular because of the variation in decay times with fluence for 400 nm probes (Figure S3d). The tens-of-picosecond decay constants in the exponential fits in Figures 4 and 5 are roughly consistent with those reported at smaller pump fluences,[22,26] which correspond to electron–phonon coupling time-scales. The signal recovery is complete at the 1.28 MHz, 5.12 MHz, and 1 kHz repetition rates of these experiments, with rapid cooling into the sapphire substrate eventually bringing the monolayer system back into its initial state. Although exact values for the interfacial thermal resistances are not known, using rough values for the heat capacity per area and typical values for interfacial thermal resistances ($\sim 10^{-6}$–10^{-7} K·m^2/W) gives a thermal time constant of order 100 ps for thermal transport into the substrate.

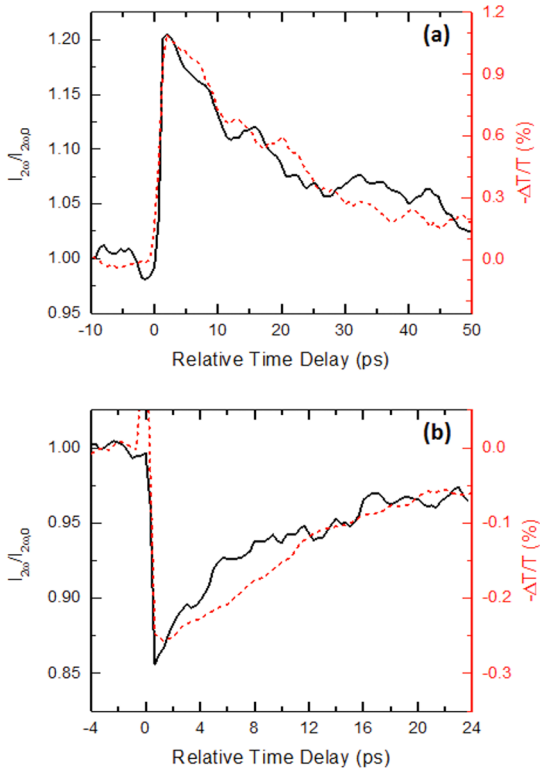

Figure 5. Time-dependent SHG (solid black lines) and linear transmission (dashed red lines) responses at equivalent absorbed pump energies. SH probe wavelengths are 1030/515 nm (a) and 800/400 nm (b). Transmission probe wavelengths are 500 nm (a) and 400 nm (b). 343 nm (a) and 266 nm (b) pump fluences for the SHG measurements were ~10 mJ/cm^2. 400 nm pump fluences for both transmission measurements were ~5 mJ/cm^2.

We note that in contrast to the extreme stability exhibited by these materials to transient photoexcitation, we do not observe similar stability under static heating. We have carried out complementary temperature-dependent transmission electron microscopy (TEM) measurements with static heating up to temperatures of order 1000 °C. These measurements show that single-domain monolayer MoS_2 undergoes an irreversible change at temperatures much lower than those we induce optically. Figure 6 shows selected-area electron diffraction patterns from monolayer MoS_2 at several different temperatures. Starting at ~900 °C, the $\{10\bar{1}0\}$ and the $\{11\bar{2}0\}$ reflections (q = 3.63 nm^{-1} and q = 6.29 nm^{-1}, respectively) begin to disappear and diffuse reflections at ~4.0 and 6.49 nm^{-1} emerge. These diffuse peaks are azimuthally broadened, suggesting decomposition into nanoscale domains with similar orientations to the original film.

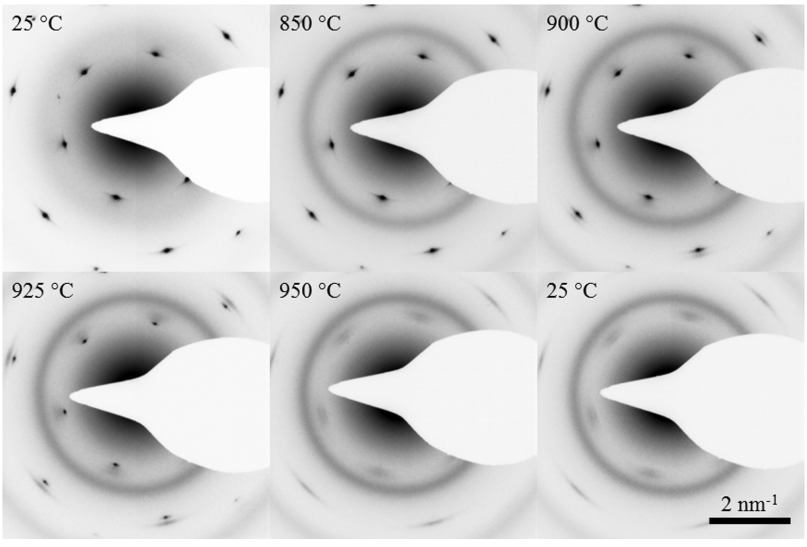

Figure 6. Selected-area electron diffraction patterns from a single-crystal domain of monolayer MoS_2 film at 25, 850, 900, 925, 950 °C, and cooled back to 25 °C. It can be seen that the film begins to undergo an irreversible transition starting at ~900 °C. The sharp reflections from the MoS_2 single crystal begin to disappear while more diffuse reflections in the same orientation but corresponding to smaller *d*-spacings begin to emerge. The diffuse ring in all images is from the ultrathin amorphous carbon film supporting the MoS_2 monolayer.

The diffuse peak at ~4.0 $Å^{-1}$ is additionally split, suggesting symmetry breaking. At ~950 °C, the decomposition is complete and does not recover upon cooling back to room temperature. Molecular dynamics simulations also indicate that monolayer MoS_2 should rapidly decompose when heated to high temperatures (see Supporting Information, Part 5).

CONCLUSIONS

In summary, we present first measurements of the time-dependent structural and electronic response of MoS_2 monolayers following intense above-bandgap excitation at megahertz repetition rates. This excitation regime corresponds to approximately one absorbed photon per unit cell (~10^{15}/cm^2) and transient temperature increases of a few thousand degrees Kelvin. We observe an increase in $\chi^{(2)}$ associated with the contribution of photoexcited carriers to an effective conduction band free electron susceptibility, with the magnitude of the modulation saturating at ~10 mJ/cm^2 excitation fluence. No evidence for disordering, decomposition, or structural rearrangements is observed at any excitation fluence presented here. These measurements open up new opportunities for dynamic control of the electronic and optical properties of two-dimensional transition metal dichalcogenides under excitation conditions not sustainable in bulk systems.

MATERIALS AND METHODS

Large-area, single-crystal domain monolayers of MoS_2 were obtained by chemical vapor deposition (CVD)-growth on sapphire substrates using MoO_3 and S as precursors.[56] We confirmed the thickness of the MoS_2 samples with a combination of optical (Figures 1b, S2) and second-harmonic microscopies (Figure S1) as well as selected area electron diffraction (Figure 5). For the second-harmonic microscopy, we use a 500 fs Yb-doped fiber laser with a 1.28-MHz repetition rate, 2 W average power, and fundamental wavelength of 1030 nm (1.20 eV, below the direct bandgap of 1.9 eV for monolayer MoS_2) in a pump−probe geometry (Figure 1a). The probe beam is focused to a 1 μm diameter onto the sample (mounted on a piezoelectric stage) within a single crystalline domain (Figure 1b) at normal incidence by a 100× objective (NA 1.30) and immersion oil with refractive index 1.518. The transmitted signal is recollimated by a 13× UV objective (NA 0.13) and reflected by a dichroic mirror through a bandpass filter centered at the second harmonic (SH) wavelength (λ = 515 nm, 2.41 eV) to remove the transmitted fundamental and any ambient light. The SH signal is then detected by a photon counting photomultiplier tube and read out by a gated photon counter synchronized to the laser repetition rate. A half wave plate is used to rotate the polarization of the incident probe light with respect to the crystallographic orientation of the sample. For the time-resolved study, we split off a portion of the laser beam and frequency-triple (λ = 343 nm, 3.62 eV) the split-off beam in two nonlinear optical crystals (LBO/BBO) to create the pump beam. This is focused to a 2 μm spot size on the sample antiparallel to the probe beam by the same 13× UV objective that recollimates the SH signal. An electron-multiplying CCD camera allows for monitoring of the positions and spatial overlap of the sample and pump and probe beams. Additional pump−probe measurements using a 50 fs Ti:sapphire laser with a 5.12 MHz repetition rate, 2 W average power, and fundamental wavelength of 800 nm (1.55 eV, also below the direct gap of monolayer MoS_2) utilized the same microscope and photon-detection setup with dichroic mirrors and band-pass filters appropriate for 400 nm (3.10 eV) in place. The third harmonic (λ = 266 nm, 4.66 eV) was used as the pump beam. Complementary measurements of the static and time-dependent linear optical response both below and above bandgap were carried out within large area monolayer films grown by using $MoCl_5$ and S as precursors[57] using a 1 kHz Ti:sapphire-based regenerative amplifier system with white light probe (see Supporting Information).

In all experiments, we observe negligible signal from the bare sapphire substrate. The damage threshold was observed to be >14 mJ/cm^2 for the 343 nm pump (the immersion oil degraded before the MoS_2 was damaged), ~15 mJ/cm^2 for the 266 nm pump, and ~10 mJ/cm^2 for the 400 nm pump. Above the damage threshold, the films were ablated away, and any signal went to zero.

Conflict of Interest: The authors declare no competing financial interest.

Acknowledgment. This work is supported by the US Department of Energy, Basic Energy Science, Materials Science and Engineering Division. Computations were supported in part by NASA Space Technology Research Fellowship (NNX12AM48H) and were performed in part with the computational resources of the National Energy Research Scientific Computing (NERSC) Center, supported by the Office of Science and the United States Department of Energy (DE-AC02-05CH11231). Part of this work was performed at the Stanford Nano Center (SNC)/Stanford Nanocharacterization Laboratory (SNL) part of the Stanford Nano Shared Facilities. L. Cao acknowledges the support by a Young Investigator Award from the Army Research Office (W911NF-13-1-0201).

Supporting Information Available: Symmetry of the SH polarization, linear absorption measurements, THz transmission measurements, electronic structure calculations, *ab initio* molecular dynamics calculations, and figures. This material is available free of charge *via* the Internet at http://pubs.acs.org.

REFERENCES AND NOTES

1. Mak, K. F.; Lee, C.; Hone, J.; Shan, J.; Heinz, T. F. Atomically Thin MoS_2: A New Direct-Gap Semiconductor. *Phys. Rev. Lett.* **2010**, *105*, 136805.
2. Splendiani, A.; Sun, L.; Zhang, Y.; Li, T.; Kim, J.; Chim, C.-Y.; Galli, G.; Wang, F. Emerging Photoluminescence in Monolayer MoS_2. *Nano Lett.* **2010**, *10*, 1271–1275.
3. Britnell, L.; Ribeiro, R. M.; Eckmann, A.; Jalil, R.; Belle, B. D. D.; Mishchenko, A.; Kim, Y.-J. Y.-J.; Gorbachev, R. V. V; Georgiou, T.; Morozov, S. V. V; *et al.* Strong Light-Matter Interactions in Heterostructures of Atomically Thin Films. *Science* **2013**, *340*, 1311–1314.
4. Bernardi, M.; Palummo, M.; Grossman, J. C. Extraordinary Sunlight Absorption and One Nanometer Thick Photovoltaics Using Two-Dimensional Monolayer Materials. *Nano Lett.* **2013**, *13*, 3664–3670.
5. Voiry, D.; Yamaguchi, H.; Li, J.; Silva, R.; Alves, D. C. B.; Fujita, T.; Chen, M.; Asefa, T.; Shenoy, V. B.; Eda, G.; *et al.* Enhanced Catalytic Activity in Strained Chemically Exfoliated WS_2 Nanosheets for Hydrogen Evolution. *Nat. Mater.* **2013**, *12*, 850–855.
6. Yu, Y.; Huang, S.-Y.; Li, Y.; Steinmann, S. N.; Yang, W.; Cao, L. Layer-Dependent Electrocatalysis of MoS_2 for Hydrogen Evolution. *Nano Lett.* **2014**, *14*, 553–558.
7. Eda, G.; Fujita, T.; Yamaguchi, H.; Voiry, D.; Chen, M.; Chhowalla, M. Coherent Atomic and Electronic Heterostructures of Single-Layer MoS_2. *ACS Nano* **2012**, *6*, 7311–7317.

8. Chang, Y. M.; Xu, L.; Tom, H. W. K. Observation of Coherent Surface Optical Phonon Oscillations by Time-Resolved Surface Second-Harmonic Generation. *Phys. Rev. Lett.* **1997**, *78*, 4649–4652.
9. Lin, Y.-C.; Dumcenco, D. O.; Huang, Y.-S.; Suenaga, K. Atomic Mechanism of the Semiconducting-to-Metallic Phase Transition in Single-Layered MoS_2. *Nat. Nanotechnol.* **2014**, *9*, 391–396.
10. Duerloo, K.-A. N.; Li, Y.; Reed, E. J. Structural Phase Transitions in Two-Dimensional Mo- and W-Dichalcogenide Monolayers. *Nat. Commun.* **2014**, *5*, 4214.
11. Bertolazzi, S.; Brivio, J.; Kis, A. Stretching and Breaking of Ultrathin MoS_2. *ACS Nano* **2011**, *5*, 9703–9709.
12. Feng, J.; Qian, X.; Huang, C. C.; Li, J. Strain-Engineered Artificial Atom as a Broad-Spectrum Solar Energy Funnel. *Nat. Photonics* **2012**, *6*, 866–872.
13. Yu, D.; Feng, J.; Hone, J. Elastically Strained Nanowires and Atomic Sheets. *MRS Bull.* **2014**, *39*, 157–162.
14. van der Zande, A.; Hone, J. Inspired by Strain. *Nat. Photonics* **2012**, *6*, 804–806.
15. Xiao, D.; Liu, G.-B.; Feng, W.; Xu, X.; Yao, W. Coupled Spin and Valley Physics in Monolayers of MoS_2 and Other Group-VI Dichalcogenides. *Phys. Rev. Lett.* **2012**, *108*, 196802.
16. Mak, K. F.; He, K.; Shan, J.; Heinz, T. F. Control of Valley Polarization in Monolayer MoS_2 by Optical Helicity. *Nat. Nanotechnol.* **2012**, *7*, 494–498.
17. Duerloo, K.-A. N.; Ong, M. T.; Reed, E. J. Intrinsic Piezoelectricity in Two-Dimensional Materials. *J. Phys. Chem. Lett.* **2012**, *3*, 2871–2876.
18. Li, Y.; Rao, Y.; Mak, K. F.; You, Y.; Wang, S.; Dean, C. R.; Heinz, T. F. Probing Symmetry Properties of Few-Layer MoS_2 and H-BN by Optical Second-Harmonic Generation. *Nano Lett.* **2013**, *13*, 3329–3333.
19. Kumar, N.; Najmaei, S.; Cui, Q.; Ceballos, F.; Ajayan, P. M.; Lou, J.; Zhao, H. Second Harmonic Microscopy of Monolayer MoS_2. *Phys. Rev. B: Condens. Matter Mater. Phys.* **2013**, *87*, 161403.
20. Kumar, N.; Cui, Q.; Ceballos, F.; He, D.; Wang, Y.; Zhao, H. Exciton-Exciton Annihilation in $MoSe_2$ Monolayers. *Phys. Rev. B: Condens. Matter Mater. Phys.* **2014**, *89*, 125427.
21. Cui, Q.; Ceballos, F.; Kumar, N.; Zhao, H. Transient Absorption Microscopy of Monolayer and Bulk WSe_2. *ACS Nano* **2014**, *8*, 2970–2976.
22. Wang, R.; Ruzicka, B. A.; Kumar, N.; Bellus, M. Z.; Chiu, H.-Y.; Zhao, H. Ultrafast and Spatially Resolved Studies of Charge Carriers in Atomically Thin Molybdenum Disulfide. *Phys. Rev. B: Condens. Matter Mater. Phys.* **2012**, *86*, 45406.
23. Wang, K.; Wang, J.; Fan, J.; Lotya, M.; O'Neill, A.; Fox, D.; Feng, Y.; Zhang, X.; Jiang, B.; Zhao, Q.; *et al.* Ultrafast Saturable Absorption of Two-Dimensional MoS_2 Nanosheets. *ACS Nano* **2013**, *7*, 9260–9267.
24. Wang, Q.; Ge, S.; Li, X.; Qiu, J.; Ji, Y.; Feng, J.; Sun, D. Valley Carrier Dynamics in Monolayer Molybdenum Disulfide from Helicity-Resolved Ultrafast Pump-Probe Spectroscopy. *ACS Nano* **2013**, *7*, 11087–11093.
25. Yang, L.; Zhong, D.; Zhang, J.; Yan, Z.; Ge, S.; Du, P.; Jiang, J.; Sun, D.; Wu, X.; Fan, Z.; *et al.* Optical Properties of Metal-Molybdenum Disulfide Hybrid Nanosheets and Their Application for Enhanced Photocatalytic Hydrogen Evolution. *ACS Nano* **2014**, *8*, 6979–6985.
26. Shi, H.; Yan, R.; Bertolazzi, S.; Brivio, J.; Gao, B.; Kis, A.; Jena, D.; Xing, H. G.; Huang, L. Exciton Dynamics in Suspended Monolayer and Few-Layer MoS_2 2D Crystals. *ACS Nano* **2013**, *7*, 1072–1080.
27. The lattice temperature jump was estimated using the specific heat of bulk MoS_2 of 1.89 J cm^{-3} K^{-1}.
28. Shank, C.; Yen, R.; Hirlimann, C. Femtosecond-Time-Resolved Surface Structural Dynamics of Optically Excited Silicon. *Phys. Rev. Lett.* **1983**, *51*, 900–902.
29. Lindenberg, A. M.; Larsson, J.; Sokolowski-Tinten, K.; Gaffney, K. J.; Blome, C.; Synnergren, O.; Sheppard, J.; Caleman, C.; Macphee, a. G.; Weinstein, D.; *et al.* Atomic-Scale Visualization of Inertial Dynamics. *Science* **2005**, *308*, 392–395.
30. Shumay, I.; Höfer, U. Phase Transformations of an InSb Surface Induced by Strong Femtosecond Laser Pulses. *Phys. Rev. B: Condens. Matter Mater. Phys.* **1996**, *53*, 15878–15884.
31. Malard, L. M.; Alencar, T. V.; Barboza, A. P. M.; Mak, K. F.; de Paula, A. M. Observation of Intense Second Harmonic Generation from MoS_2 Atomic Crystals. *Phys. Rev. B: Condens. Matter Mater. Phys.* **2013**, *87*, 201401.
32. Wagoner, G. A.; Persans, P. D.; Van Wagenen, E. A.; Korenowski, G. M. Second-Harmonic Generation in Molybdenum Disulfide. *J. Opt. Soc. Am. B* **1998**, *15*, 1017–1021.
33. Ulbricht, R.; Hendry, E.; Shan, J.; Heinz, T. F.; Bonn, M. Carrier Dynamics in Semiconductors Studied with Time-Resolved Terahertz Spectroscopy. *Rev. Mod. Phys.* **2011**, *83*, 543–586.
34. Ashcroft, N. W.; Mermin, N. D. *Solid State Physics*; Holt, Rinehart and Winston: Boston, 1976.
35. Glezer, N.; Siegal, Y.; Huang, L.; Mazur, E. Behavior of $\chi^{(2)}$ During a Laser-Induced Phase Transition in GaAs. *Phys. Rev. B: Condens. Matter Mater. Phys.* **1995**, *51*, 9589–9596.
36. Akhmanov, S. A.; Koroteev, N. I.; Paitian, G. A.; Shumay, I. L.; Galjautdinov, M. F.; Khaibullin, I. B.; Shtyrkov, E. I. Pulsed-Laser Annealing of GaAs Surface Studied by Time-Resolved Second Harmonic Generation in Reflection. *Opt. Commun.* **1983**, *47*, 202–204.
37. Guo, C.; Rodriguez, G.; Taylor, A. Ultrafast Dynamics of Electron Thermalization in Gold. *Phys. Rev. Lett.* **2001**, *86*, 1638–1641.
38. Guo, C.; Rodriguez, G.; Hoffbauer, M.; Taylor, A. J. Influence of Electronic Temperature and Distribution on the Second-Order Surface Nonlinear Susceptibility of Metals. *Appl. Phys. Lett.* **2001**, *78*, 3211.
39. Papadogiannis, N. A.; Moustaizis, S. D. Nonlinear Enhancement of the Efficiency of the Second Harmonic Radiation Produced by Ultrashort Laser Pulses on a Gold Surface. *Opt. Commun.* **1997**, *137*, 174–180.
40. Bodlaki, D.; Borguet, E. Dynamics and Second-Order Nonlinear Optical Susceptibility of Photoexcited Carriers at Si(111) Interfaces. *Appl. Phys. Lett.* **2003**, *83*, 2357.
41. McClelland, A.; Fomenko, V.; Borguet, E. Ultrafast Time-Evolution of the Nonlinear Susceptibility of Hot Carriers at the Ge(111)−GeO_2 Interface As Probed by SHG. *J. Phys. Chem. B* **2004**, *108*, 3789–3793.
42. McClelland, A.; Fomenko, V.; Borguet, E. Ultrafast Hot-Carrier Dynamics at Chemically Modified Ge Interfaces Probed by SHG. *J. Phys. Chem. B* **2006**, *110*, 19784–19787.
43. Johnson, J. C.; Knutsen, K. P.; Yan, H.; Law, M.; Zhang, Y.; Yang, P.; Saykally, R. J. Ultrafast Carrier Dynamics in Single ZnO Nanowire and Nanoribbon Lasers. *Nano Lett.* **2004**, *4*, 197–204.
44. Son, D.; Wittenberg, J.; Banin, U.; Alivisatos, A. Second Harmonic Generation and Confined Acoustic Phonons in Highly Excited Semiconductor. *J. Phys. Chem. B* **2006**, *110*, 19884–19890.
45. Boyd, R. W. *Nonlinear Optics*; Academic Press: Waltham, MA, 2008.
46. Sharma, S.; Dewhurst, J. K.; Ambrosch-Draxl, C. Linear and Second-Order Optical Response of III-V Monolayer Superlattices. *Phys. Rev. B: Condens. Matter Mater. Phys.* **2003**, *67*, 165332.
47. Dewhurst, K.; Sharma, S.; Nordstrom, L.; Cricchio, F.; Bultmark, F.; Granas, O.; Gross, H.; Ambrosch-Draxl, C.; Persson, C.; Brouder, C.; *et al.* Elk Code, v. 2.3.22; 2014. http://elk.sourceforge.net.
48. Hughes, J. L. P.; Sipe, J. E. Calculation of Second-Order Optical Response in Semiconductors. *Phys. Rev. B: Condens. Matter Mater. Phys.* **1996**, *53*, 10751.
49. Shi, H.; Pan, H.; Zhang, Y.-W.; Yakobson, B. Quasiparticle Band Structures and Optical Properties of Strained Monolayer MoS_2 and WS_2. *Phys. Rev. B: Condens. Matter Mater. Phys.* **2013**, *87*, 155304.
50. Qiu, D. Y.; da Jornada, F. H.; Louie, S. G. Optical Spectrum of MoS_2: Many-Body Effects and Diversity of Exciton States. *Phys. Rev. Lett.* **2013**, *111*, 216805.

51. Alfè, D.; Pozzo, M.; Desjarlais, M. P. Lattice Electrical Resistivity of Magnetic Bcc Iron from First-Principles Calculations. *Phys. Rev. B: Condens. Matter Mater. Phys.* **2012**, *85*, 24102.
52. Knyazev, D. V.; Levashov, P. R. Ab Initio Calculation of Transport and Optical Properties of Aluminum: Influence of Simulation Parameters. *Comput. Mater. Sci.* **2013**, *79*, 817–829.
53. Clérouin, J.; Mazevet, S. Exploring Warm Dense Matter Using Quantum Molecular Dynamics. *J. Phys. IV* **2006**, *133*, 1071–1075.
54. Sharma, S.; Ambrosch-Draxl, C. Second-Harmonic Optical Response from First Principles. *Phys. Scr.* **2004**, *2004*, 128.
55. Ge, S.; Liu, X.; Qiao, X.; Wang, Q.; Xu, Z.; Qiu, J.; Tan, P.-H.; Zhao, J.; Sun, D. Coherent Longitudinal Acoustic Phonon Approaching THz Frequency in Multilayer Molybdenum Disulphide. *Sci. Rep.* **2014**, *4*, 5722.
56. Lee, Y.-H.; Zhang, X.-Q.; Zhang, W.; Chang, M.-T.; Lin, C.-T.; Chang, K.-D.; Yu, Y.-C.; Wang, J. T.-W.; Chang, C.-S.; Li, L.-J.; *et al.* Synthesis of Large-Area MoS_2 Atomic Layers with Chemical Vapor Deposition. *Adv. Mater.* **2012**, *24*, 2320–2325.
57. Yu, Y.; Li, C.; Liu, Y.; Su, L.; Zhang, Y.; Cao, L. Controlled Scalable Synthesis of Uniform, High-Quality Monolayer and Few-Layer MoS_2 Films. *Sci. Rep.* **2013**, *3*, 1866.